AN INTEGRAL EQUATION METHOD FOR DUAL-WAVELENGTH RADAR DATA USING A WEAK CONSTRAINT

5A.2 Robert Meneghini[1] and Liang Liao[2]

[1]NASA/Goddard Space Flight Center, [2]Goddard Earth Sciences & Technology Center

1. ABSTRACT

A set of integral equations for dual-wavelength radar data provides a means of estimating liquid water content and parameters of the particle size distribution (PSD) [Meneghini et al., 1997] and constitutes a potential algorithm for the proposed DPR (Dual-wavelength Precipitation Radar) on the Global Precipitation Mission (GPM) satellite [Iguchi et al., 2002]. One version of the method, the forward-recursion, starts at the storm top. Although this implementation requires no constraint, like the Hitschfeld-Bordan (1954) solution, it tends to be unstable when the path attenuation becomes significant. As such, the method can be applied with confidence only in regions of frozen hydrometeors or light rain. For moderate rain or mixed-phase precipitation, the backward recursion is preferable because it is more robust. The backward recursion, however, requires constraints of path-integrated attenuation (PIA) down to the surface at both wavelengths, estimates of which have typically come from the surface reference technique (SRT).

There has been work on improving the stability of the method by constraining the behavior of the PSD parameters along the range direction. In addition, an iteration and consistency approach has been investigated with the purpose of deriving estimates that are independent of the SRT [Mardiana et al., 2004; Rose and Chandrasekar, 2006; Liao and Meneghini, 2005]. The behavior of the solutions with respect to variations in the PIA suggests an alternative to the SRT using the difference in the measured radar reflectivity factors near the surface. This difference, however, is a weak constraint in the sense that it is itself a function of one of the unknowns - the characteristic size parameter of the distribution. This implies, in turn, that there are multiple solutions consistent with the constraint. Three factors, however, may act to reduce the ambiguities. The first is that, when the attenuation is moderate or strong, the solutions often converge quickly as the solution progresses toward the storm top. A second mitigating factor is that the solution that assumes the correct or nearly correct size parameter typically exhibits the smallest variability in the rain rate and PSD parameters as the solution approaches the surface. Thirdly, out-of-range values of the size parameter can be eliminated because they lead to negative path attenuations. Thus, if we assume that the PSD parameters are smoothly varying as the surface is approached, an accurate candidate solution can sometimes be chosen, particularly if the number of independent samples is large and the μ value is close to the true value.

Some of the drawbacks and error sources of this approach, as well as comparisons to the forward and backward recursion with an SRT constraint, are discussed in the context of simulated and experimental airborne radar data.

2. INTRODUCTION & BACKGROUND

The essence of the dual-wavelength approach that will be considered here is that information of the particle size distribution (PSD) can be inferred from non-Rayleigh scattering effects, or more precisely, by the differential non-Rayleigh scattering between the two frequencies. The key to this is the relationship between the dual-wavelength ratio, DFR, and the characteristic size parameter of the PSD. Like ZDR in the dual-polarization methods, the DFR is independent of the particle number

* Robert Meneghini, NASA/Goddard Space Flight Center, Code 613.1, Greenbelt, MD 20771; email: Robert.Meneghini-1@nasa.gov

concentration, N_t, so that with fixed shape parameter μ in the gamma distribution, the median mass diameter, D_0, or a similar parameter like mass-weighted diameter, can be estimated from the DFR. However, for typical spaceborne weather radar or cloud radar frequencies (Ku-band and above), attenuation must be corrected before the method can be applied. For the method considered here, the attenuations are expressed in terms of the PSD parameters at previous range gates so the equations for D_0 and N_t take the form of integral equations that can be solved either forward (from the storm top down) or backwards (from the surface up). In the latter case, path-integrated attenuations (PIA) are needed to start the recursion. This can be done either by the use of the surface reference technique or by an arbitrary assumption regarding the attenuations which are then used as the first step in an iteration. The approach examined here considers the reflectivity factor difference near the surface and its relationship to the differential path attenuation. This provides a set of weak constraints on the backward recursion solution. In the following section, this is described in more detail. In section 3, the behavior of the technique is shown using a simple simulation. In section 4, the analysis is carried out using dual-wavelength radar data from the JPL APR2 airborne radar.

3. NEAR-SURFACE WEAK CONSTRAINT

Expressing all quantities in dB, the DFR is related to the radar reflectivities, Z, at range r by

$$DFR(r) = Z(f_1, r) - Z(f_2, r) \equiv \delta Z(r) \qquad (1)$$

Where $f_1<f_2$ which for the frequencies of interest (f_1=13.6, f_2=35.5 GHz) ensures that the DFR is always positive for snow and positive for rain for most values of D_0 and μ. The measured radar reflectivity, Z_m, and attenuation, A, are related to Z by:

$$Z(f,r) = Z_m(f,r) + 2\int_0^r k(f,s)ds \equiv Z_m(f,r) + A(f,r) \qquad (2)$$

Combining (1) and (2) gives

$$DFR(r) = \delta Z_m(r) + \delta\tilde{A}(r) \qquad (3)$$

where $\delta\tilde{A}(r)$ =A(f_1,r)-A(f_2,r) and $\delta Z_m(r)$ =Z_m(f_1,r)-Z_m(f_2,r). The dual-wavelength method proceeds by expressing the differential attenuation (dB) in terms of parameters of the PSD obtained at prior gates. When the solution is run forward, from the storm top, δA(r=0) =0; when the solution begins near the surface, at range r_s^-, then $\delta A(r=r_s^-)$ must be specified, where r_s^- is used to denote the gate just above the surface. Note that for the SRT, the attenuations are specified at the surface gate itself. To understand the weak constraint, it is convenient to write (3) in a slightly different form, evaluated at $r = r_s^-$

$$\delta A(r_s^-) = \delta Z_m(r_s^-) - DFR(r_s^-) \qquad (4)$$

Where $\delta A(r_s^-) = -\delta\tilde{A}(r_s^-) > 0$

Eq. (4) states that the differential path attenuation is equal to the difference between the differential measured radar reflectivity factor and the DFR. But as noted above, the DFR is independent of the particle number concentration, N_t, and depends only on D_0 and μ. This implies that for each assumed (D_0, μ), the DFR can be evaluated so that, since $\delta Z_m(r_s^-)$ is a measured quantity, the differential path attenuation, $\delta A(r_s^-)$, can be obtained. From the $\delta A(r_s^-)$, the PIA at the lower or higher frequency can be estimated. This, along with the D_0 estimate, provides the information needed to perform the backward recursion from the surface to the storm top. For example, if we fix μ and let D_0 take on n possible values at the near-surface gate, then we can obtain n

corresponding pairs of (δPIA, PIA(f_2)) which can be used in the backward recursion to produce n candidate profiles of the PSD.

4. SIMULATION RESULTS

The simulation is performed by first assuming a range profile of the rain PSD parameters D_0, N_t, for fixed μ, over a 4.5 km path. Using a range gate length of 0.3 km, we generate the data: $[\{Z_m(f_i, r_j), j=1, 150, i=1,2\}_k, k=1,500]$, where the quantities in the inner bracket represent a single dual-wavelength profile. For each PSD, five-hundred such profiles (k=1,..,500) are generated to study the variability of the Z_m and its affect on the retrieval. This variability depends on the number of independent samples and the radar receiver, which in this case is assumed to be logarithmic. To test the weak constraint approach outlined above, each 'retrieval' now consists of 10 'sub-retrievals' that correspond to 10 D_0 estimates at the final gate. These have been assumed to range from 1 mm to 2.8 mm in steps of 0.2 mm. Note that the path-attenuation estimates in these cases come directly from the differential Z_m data at the final gate (gate 150) in the path, just above the presumed surface. In the results below, we show only the mean values from the 10 sub-retrievals and not the associated standard deviations.

The heavy solid lines in the 3 panels of Fig. 1 show the input profiles of D_0 (center panel), N_t (bottom panel) and the resultant rain rate (top panel) for an assumed μ of 2. For this example, the input or true D_0 profile is assumed to increase from 1.4 mm at the 'storm top' (0 km range) to 1.8 mm at the gate just above the surface (4.5 km range). The input N_t is assumed to decrease slightly from 500 m^{-3} to 450 m^{-3} over the same range interval. Nine of the ten profiles generated from the 10 D_0 assumptions can be clearly distinguished in the center (D_0) plot at r=4.5 km: starting from the lower-most curve, the light solid line corresponds to D_0(r=4.5 km) = 1 mm, the light dotted line to D_0(r=4.5 km) = 1.2 mm, etc. The retrieval corresponding to the D_0(r=4.5 km)= 1.8 mm assumption is hidden by the true value result since it corresponds to the true or input D_0 value. Several features of the results are worth noting. As the solutions are tracked up to the storm top, the majority of them tend to converge to the same set of results and that these results are close to the input profiles of D_0, N_t and R. Secondly, of the ten candidate solutions generated, the solution with the smoothest behavior (i.e., smallest second derivative with respect to range) near the surface or end point of the interval, is the true solution – i.e., that solution that is in best agreement with the input PSD profile.

For the results in Fig. 1, the number of independent samples, N, is assumed to be 1000. If this is reduced to N=100, the results shown in Fig. 2 are obtained. This leads to a degradation of the retrievals in several respects. The D_0-solution curves do not converge as well as in the previous case. Moreover, the N_t curves show divergence rather than convergence as the solutions are tracked toward the rain top. Note also that the N_t curve that corresponds to the true D_0 input (the dash-dot-dot curve), while starting at the near-surface gate close to the true value, exhibits an increasingly positive bias toward the storm top. Despite these errors, the rain rate solutions remain fairly good in that the errors in D_0 and N_t tend to compensate because the solutions must be consistent with the input Z_m data. As a consequence of this, the retrievals tend to be consistent with higher moments of the PSD, including rain rate.

As the attenuation increases, the convergence properties of the solutions generally improve. This is shown in Fig. 3. In this case, the input D_0 profile is assumed to increase from 1.7 mm (storm top) to 2.1 mm (near-surface) while the N_t, as before, is assumed to decrease from 500 m^{-3} to 450 m^{-3}. In this case, there is a more rapid convergence of the curves as the solutions proceed toward the storm top. Despite this

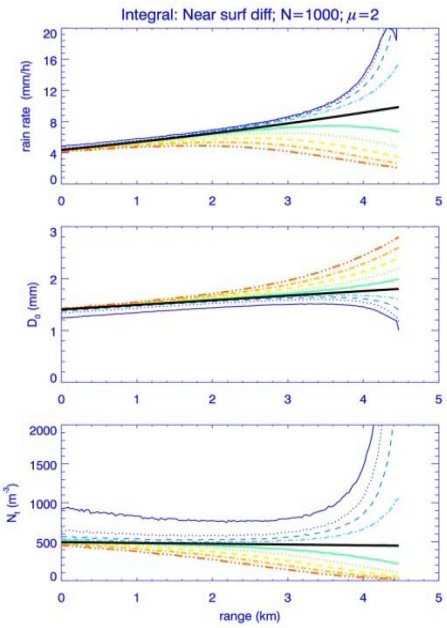

Fig. 1. Black heavy lines represent input values of R, D_0 and N_t. Colored lines represent the weakly-constrained retrieved profiles for values of D_0(rs) from 1 to 2.8 mm.

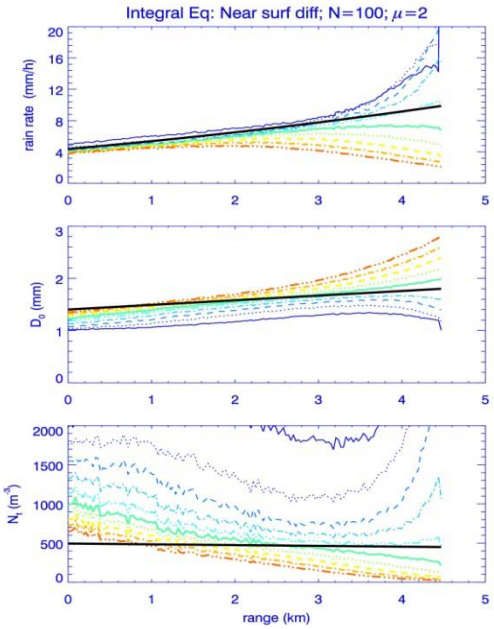

Fig. 2. Same as Fig. 1 but for number of independent samples of 100 rather than 1000.

feature, the curves tend toward D_0 values that are slightly negatively biased and N_t that are positively biased despite unbiased rain rate estimates. The reason for this behavior can be traced to the coefficient in the k-δk relation. A slight increase in the slope improves the behavior of solutions at high D_0 values but degrades the behavior at lower D_0 values. In fact, using disdrometer-measured raindrop size distributions, it is straightforward to obtain coefficients of the k-δk fit that are functions of D_0. Even though the fits are generally good, with small standard errors, even small errors will affect the retrieval in high attenuation cases. It should be kept in mind that while the PSDs in the simulation are based on typical values of D_0, N_t, μ, the k-δk fits obtained from disdrometer-measured DSDs may not be appropriate for the simulated data.

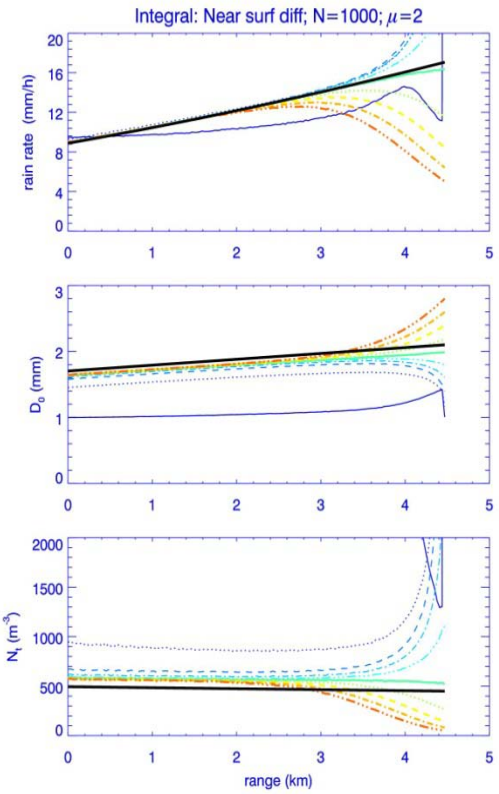

Fig. 3. Same as Fig. 1 but for higher rain rate.

A final example of the approach is shown in Fig. 4. This is a light rain rate case where D_0 is assumed to decrease linearly from 1.4 mm at r=0 km to 1.1 mm at r=4.5 km while N_t increases from 500 m^{-3} to 550 m^{-3} over this interval. As in the previous case, the set of assumed D_0's do not equal the true value at the final gate since $D_{0,\ true}$(4.5 km) = 1.1 mm whereas the assumed values of D_0 closest to this are at 1 mm and 1.2 mm. Despite this, the two profiles corresponding to these initial assumptions (shown by the light solid and dotted curves in each of the panels) begin and remain close to the true profiles. One other feature of the results worth noting is that the 10 solution curves in this case are not distinct: profiles corresponding to the initial D_0 values of (2.2, 2.4, 2.6, 2.8) mm become the same because in this case because for D_0(4.5 km)> 2.2 mm, DFR(r_s^-)>$\delta Z_m(r_s^-)$ (see eq. (4)) which leads to negative path-integrated attenuations. Because this is not physically possible, the path attenuations are set to zero and all profiles with a final value of D_0(4.5 km) > 2.2 mm are identical. Although the final-values of D_0 that are approximately correct in this case lead to accurate range-profiles of D_0, N_t, and R, most of the solution curves are nearly straight lines and the convergence of the solutions, particularly in the N_t and R spaces, is weak. On the other hand, the N_t plots show that all but three solutions tend to values that are nearly 0 near the endpoint of the interval. If we reject all but the three solutions that provide reasonable N_t values we are left with this three-fold ambiguity. Although the solution corresponding to D_0(4.5 km)=1 mm can be rejected because of the instability in N_t near the surface, it is clear that for light rain rate cases, the choice of solution is not obvious and ambiguities remain.

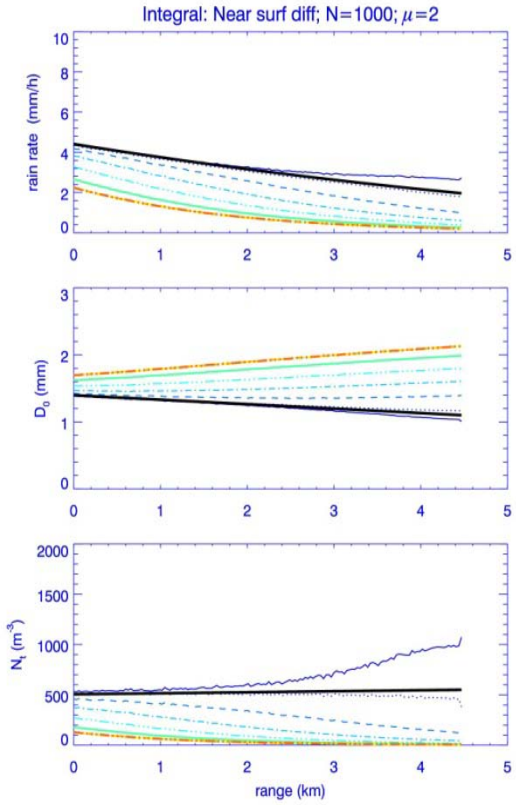

Fig. 4. Light rain rate case with similar conventions as other figures.

5. EXPERIMENTAL RESULTS

The JPL APR2 airborne dual-wavelength radar [Im et al., 2000; Tanelli et al., 2006] operates at 13.4 and 35.6 GHz, and serves as a simulator for the DPR, the dual-wavelength spaceborne Precipitation Radar being built by JAXA of Japan for the Global Precipitation Mission. The APR2 has Doppler and HH and HV polarization capabilities at both channels and provides cross-track data $\pm 25^0$ of nadir using approximately matched beamwidths of about 4^0. The data investigated here were acquired on 1 September 2006 during the NAMMA (NASA African Monsoon Multi-disciplinary Analysis) field campaign experiment. Measurements of Z_m(Ku) and Z_m(Ka) at nadir are shown in Fig. 5 over a 120 km flight leg over an ocean background. Note the presence of a melting layer at a height of about 4.3 km and a strong surface return terminating the path. Because the radar employs a pulse compression technique, and because of the presence of strong surface

clutter at nadir, the surface clutter masks the lowest ~0.5 km of the rain just above the surface.

In investigating the retrieval methods for these data, it is convenient to consider small, intermediate and large values of $\delta Z_m(r_s^-)$ since this magnitude determines the general behavior of the solutions. As noted in the simulation example, for small values of $\delta Z_m(r_s^-)$, the values of $D_0(r_s)$ are restricted. This can be understood by noting that large D_0 will produce a large $\delta Z_m(r_s^-)$ and that the differential path attenuation will further add to the observed δZ_m. Conversely, a small observed $\delta Z_m(r_s^-)$ places an upper limit on D_0. Since $\delta A>0$, then a upper bound for D_0 is that value for which $DFR(D_0(r_s^-)) = \delta Z_m(r_s^-)$. A more stringent upper bound on D_0 can be obtained by using a lower bound in a δk-Z(Ku) power law relationship and by using the fact that $Z_m(Ku)<Z(Ku)$. Using this δk-$Z_m(Ku)$ power law provides a lower bound on δA, δA_{LB}

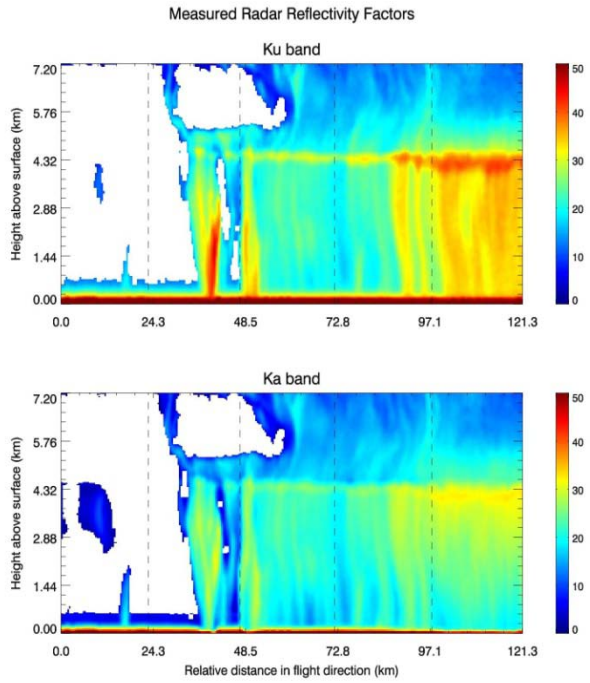

Fig. 5. JPL APR2 measured radar reflectivity factors at nadir for 13.4 GHz (top) and 35.5 GHz (bottom) for ~120 km flight leg taken on 1 September 2006.

so that an upper bound on D_0 is given by the solution to the equation: $DFR(D_0(r_s^-)) = \delta Z_m(r_s^-) - \delta A_{LB}(r_s^-)$. An example of a small $\delta Z_m(r_s^-)$ is shown in Fig. 6 where zero range is taken to be the storm top and the melting layer maxima occur at about 2.8 km. The corresponding retrievals for D_0 and N_t are shown in Fig. 7. In this case, most of the retrievals are co-aligned and it is difficult to distinguish them. Note that the red curve corresponds to the forward recursion result while the black curve, partially hidden, corresponds to the backward recursion using the SRT. The maximum D_0 assumption, corresponding to the green curve, is 1.4 mm; values larger than this correspond to non-physical solutions where the differential path attenuation is negative. Lower values of $D_0(r_s^-)$ are possible, however, and lead to lower D_0 values and higher N_t values along the full profile.

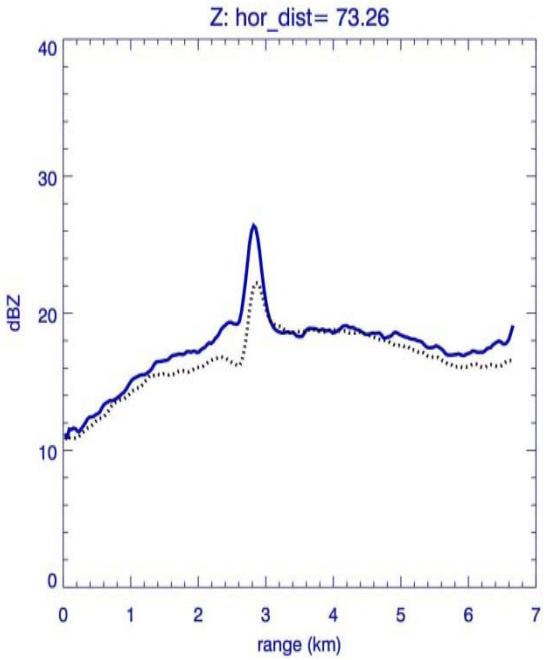

Fig. 6. Measured reflectivity factors, Z_m, at Ku-band (solid) and Ka-band (dotted) at 73.3 km measured along flight leg shown in Fig. 5.

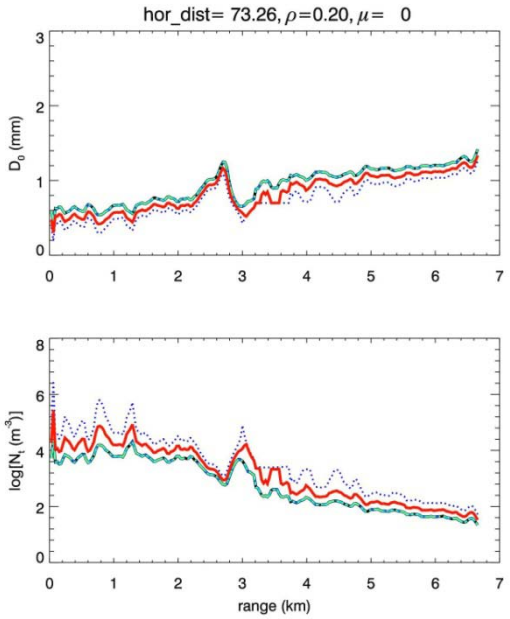

Fig. 7. Retrieved range profiles of D_0 (top) and N_t for case shown in Fig. 6. Note that the D_0 is the melted median diameter at all ranges.

The measured radar reflectivities for a moderate stratiform case are shown in Fig. 8. The corresponding retrievals for D_0 and N_t are given in Fig. 9. For the profiles shown, the values of $D_0(r_s^-)$ range from 1.2 mm to 1.8 mm with step size 0.2 mm, all of which yield allowable solutions to the dual-wavelength equations. By 'allowable' we mean that the measured Z_m profiles at both frequencies can be recovered by using the derived (and assumed) parameters of the PSD if an account is made for any differences between the input and output PIAs. As in the previous example, the forward and backward recursion (using the SRT) results are given by the red and black curves, respectively. As in the simulation results of Figs. 1 and 3, all the backward solutions, including the weakly-constrained and the SRT, converge to a single D_0 and N_t profile as the solutions progress toward the storm top. However, unlike the previous example, the solutions do not closely match the forward solution in the snow layer from 0 to about 2.6 km. But since the forward solution is more 'accurate' in this region, in the sense that little or no attenuation correction is needed, we conclude that the attenuation from the melting layer region, that affects the backward solutions but not the forward solution in this region, is the most probable cause of the discrepancy.

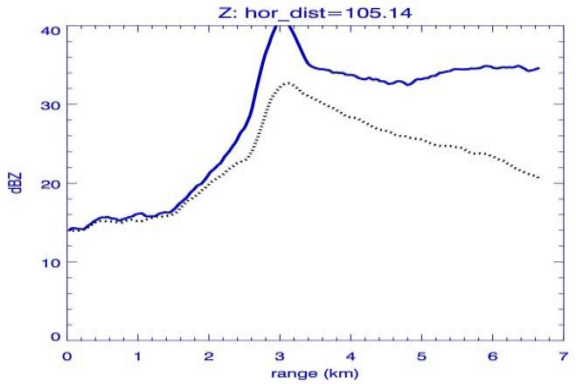

Fig. 8. Measured reflectivity factors, Z_m, at Ku-band (solid) and Ka-band (dotted) at 105.1 km.

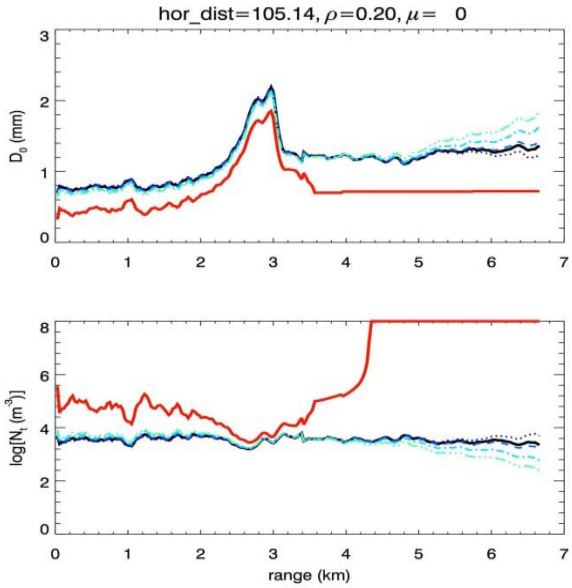

Fig. 9: Retrieved range profiles of D_0 (top) and N_t for case shown in Fig. 8.

In the final example, we show an intermediate case, similar to the simulation result given in Fig. 4, where only partial convergence of the weakly constrained solutions occur but where the forward and backward recursion results are in good agreement in the snow region. The

profiles of Z_m and the corresponding retrievals are shown below in Figs. 10 and 11.

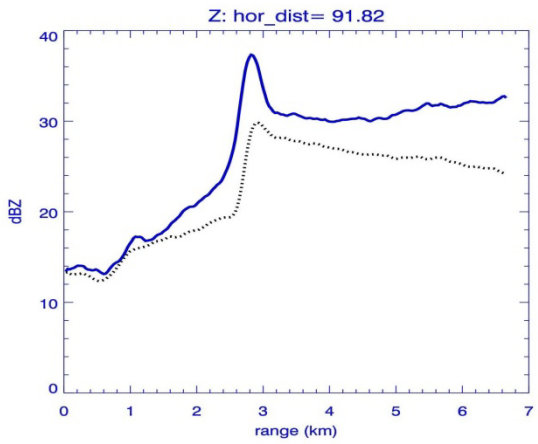

Fig. 10. Measured reflectivity factors, Z_m, at Ku-band (solid) and Ka-band (dotted) at 91.8 km.

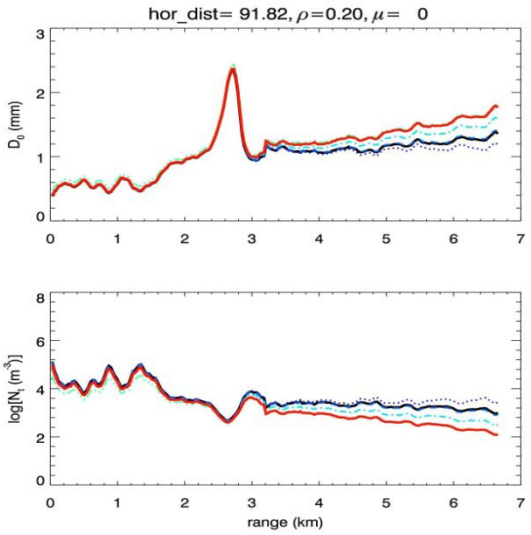

Fig. 11. Retrieved range profiles of D_0 (top) and N_t for case shown in Fig. 8.

As in the simulated case, unless additional information is known or assumed about the behavior of D_0 or N_t near the surface, it is difficult to chose a 'best' solution and while the weakly constrained solutions show the sensitivity of the D_0, N_t profiles to changes in δA, or equivalently, to changes in D_0 near the surface, they do not reduce the ambiguity of the solutions.

6. CONCLUSIONS

The dual-wavelength equations are designed to convert profiles of Z_m at two frequencies into profiles of D_0, N_t, and, ultimately into profiles of rain rate and liquid water content. However, the forward solutions tend to become unstable as the attenuation increases. Backward solutions, while more robust, require accurate estimates of the path-integrated attenuation at both frequencies. However, these are often not available from the surface reference technique. In this paper, the apparent or measured DFR near the surface, denoted by $\delta Z_m(r_s^-)$, was seen to be closely related to the differential path attenuation and the D_0 at r_s^-. These relationships can be used to generate multiple (or weakly-constrained) solutions of the backward recursion equations for D_0 and N_t. For light rain rates, using the fact that δA must be positive, the constraint is effective in excluding solutions that are inconsistent with the $\delta Z_m(r_s^-)$ measurement. For large values of $\delta Z_m(r_s^-)$, the simulated and experimental results show that the solutions usually converge to single profiles of D_0 and N_t as the solutions progress towards the storm top. Whether a single 'best' solution can be chosen on a consistent basis depends on a knowledge of the behavior of these parameters in moving toward the surface. In some cases, a number of the solutions that show strong changes in D_0 or N_t with range can be ruled out; unfortunately, this can still leave a large variance in the allowable set of solutions, especially near the surface. The forward solution holds some promise of reducing the uncertainties in the light rain rate cases and in the snow layer but is usually unstable at higher rain rates.

Acknowledgement: We wish to thank Dr. Simone Tanelli of the Jet Propulsion Laboratory for the PR2 data and helpful advice in using it.

References

Im, E., S.L. Durden, G. Sadowy, and L. Li, 2000: The tropical rainfall measuring mission (TRMM) sensor package. Proc. IGARSS '00, *IEEE Trans. Geosci. Remote Sens*.

Hitschfeld. W. and J. Bordan, 1954: Errors inherent in the radar measurement of rainfall at attenuating wavelengths. *J. Meteor*., **11**, 58-67.

Iguchi, T, R. Oki, E.A. Smith, and Y. Furuhama, 2002: Global precipitation measurement program and the development of dual-frequency precipitation radar. *J. Commun. Res. Lab. (Japan)*, **49**, 37-45.

Liao, L. and R. Meneghini, 2005: A study of air/space-borne dual-wavelength radar for estimation of rain profiles. Advances in Atmos. Sci., 22, 841-851.

Mardiana, R., T. Iguchi and N. Takahashi, 2004: A dual-frequency rain profiling method without the use of a surface reference technique. *IEEE Trans. Geosci. Remote Sens.*, **42**, 2214-2225.

Meneghini, R., H. Kumagai, J.R. Wang, T. Iguchi, and T. Kozu, 1997: Microphysical retrievals over stratiform rain using measurements from an airborne dual-wavelength radar-radiometer. *IEEE Trans. Geosci Remote Sens*., **35**, 487-506.

Rose, C.R. and V. Chandrasekar, 2006: A GPM dual-frequency retrieval algorithm: DSD profile-optimization method. *J. Atmos. Oceanic Technol.*, **23**, 1372-1383.

Tanelli. S., S. L. Durden, and E. Im, 2006: Simultaneous measurements of Ku- and Ka-band sea surface cross sections by an airborne radar. *IEEE Trans. Geosci. Remote Sens. Letters*, **3**, 359-363.